Chapter 5

Density gradients and the associated proton acceleration mechanisms in a laser exploded Gaussian-shaped plasma microsphere

An investigation is made on the influence of the sharpness of density gradients on the generation of energetic protons in a radially Gaussian density profile of a spherical Hydrogen plasma. It is possible to create such density gradients by impinging a solid density target with a secondary lower intensity pulse, which ionizes the target and explodes it to create an expanded plasma target of lower effective density for the high-intensity main pulse to hit on. The density gradients are scanned in the near-critical regime, and separate regimes of proton motion are identified based on the density sharpness. An intermediate density gradient [$n_{peak} \approx (1.5 - 2.5)\gamma n_c$] favours the generation of high energetic protons with narrow energy spectra that are emitted with better collimation from the target rear-surface. Protons with energies exceeding 100 MeVs could be achieved using such modified plasma targets with circu-

larly polarized lasers of peak intensities $I_0 \sim 10^{20} W cm^{-2}$ and peak energy $\sim 10 J$.

5.1   Motivation and background of the study

For an overdense target, the laser propagation is inhibited inside it and a density steepening induces an ion-acoustic wave whose supersonic motion may give rise to shock formation [1]. As the high-density shock-front propagates into the low density (upstream) plasma, ions having kinetic energies less than the shock potential are reflected at the shock-front and get accelerated to twice the shock velocity [2]. However, when the target is effectively transparent to the laser, a volumetric heating and subsequent expansion may cause breaking of the ion-acoustic wave at the decreasing density gradient of the expanding target [3, 4, 5]. The shock acceleration mechanism has been found to produce energetic protons with a high proton number and a narrower bandwidth. The production of such good quality proton beam can be sustained for longer periods by suppressing the effect of the sheath electric field at the rear target surface. It has been shown that a decreasing density gradient at the rear surface helps in maintaining the mono-energetic feature of the shock accelerated protons [6, 7].

The design of engineered targets such as exploded [8, 9, 10, 11], structured [12, 13, 14], foam targets [15, 16, 17], etc. have shown to result in a reduction in the average density from solid to a near-critical one ($n_e \sim \gamma n_c = \dfrac{\gamma m_e \omega^2}{4\pi e^2}$). Such targets display an increased absorption of the laser energy leading to an enhancement in the final energies of the accelerated ions [18].

In the present chapter, we have used a fully ionized spherical Hydrogen plasma target comprising solely of electrons and protons (the terms 'protons' and 'ions' represent the same entity for this work). The idea behind using pre-exploded target is to reduce the effective density of a solid target for an efficient laser-to-target energy absorption. This aim can be met comparatively easily and homogenously by using a mass-

limited spherical target. An isotropic expansion of a microsphere target also lowers the density comparatively faster than in the case of an exploded flat foil. Apart from that, the proton acceleration mechanism is also highly influenced by the use of such mass-limited targets. The limited transverse dimension facilitates the confinement of the electrons which aids the consequent acceleration and guiding of the protons.

In this chapter, 3D-PIC simulation has been performed on the spherical target that has a radially Gaussian density profile. The target is considered to be first irradiated with a secondary pulse which results in the density gradient due to an isotropic expansion. A circularly polarized high-intensity main pulse is then allowed to hit the expanded target, and by tuning the density gradients, an active parameter regime is obtained, which assists the generation of high-quality proton beams. In Chapter 3, we have found that a radially Gaussian density profile facilitates the production of high energetic proton bunches. In the present chapter, our aim is to identify the dominant acceleration schemes by tuning the target density gradient and establish an efficient steepness of the density where strong proton bunches of low-divergence may be emitted. Under the best conditions, protons bunches can be accelerated to energies beyond the 100 MeV mark with beam divergence less than 15 degrees. Such energetic beams have the potential for applications (eg. in hadron therapy) upon further refinement. Unlike previous works [8, 9, 20, 21], where exploded foils were used, here, we have considered a plasma microsphere. Pre-exploding a micron-sized spherical target leads to an isotropic distribution of the plasma thereby improving the laser-to target absorption efficiency. The spherical shape speeds up the expansion process and evenly distributes the plasma, as compared to an exploded flat foil target. A spherical exploded Hydrogen target was used in the simulation study by Stockem Novo *et al* [22], where they optimized a parameter space where collisionless shock conditions were achieved and the protons were accelerated to high energies using a linearly polarized laser. In our study, we have used an exploded spherical target, and similar to [22], we found a steep density regime where CSA is the dominant acceleration mecha-

nism aided by the expanding background plasma. However, we have also defined other density regimes where the underlying proton dynamics get changed. An intermediate density regime has been identified that generates high energy protons with a laser of much less intensity compared to those reported in [22]. The novelty of this study lies in the target shape and the radially Gaussian density form that has not been explored much. In an earlier work by Hilz et al. [23, 24], a Gaussian shaped density distribution was considered in a pre-exploded plastic micro-sphere target of near-critical density. The laser and target parameter regime reported there is somewhat similar to those used in the present work. In [23] and [24], they attained a directional proton distribution which is guided due to the ponderomotive focusing of the electrons. However, the generation of strong collsionless shock was not observed there, which may be due to the lower core density. In the present work, it is found that shape and the density profile helps in a better heating as the target mostly remains relativistically transparent for the laser pulse. This strong volumetric heating later triggers the density shocks, which reflect upstream protons to high velocities. In this work, we have identified three density regimes, i.e. a low gradient, an intermediate gradient, and a high gradient, where three separate proton actions are manifested. Since we have kept the target size (the full-width at half maxima) constant throughout, in our context the density gradient can be controlled by changing the peak density of the core. A high density gradient is created by increasing the density of the core and vice-versa.

5.2   PIC simulation model

The simulations are performed using the relativistic 3D PIC code Picpsi-3D [25], where we use a femtosecond pulsed, circularly polarised laser that hit a spherical hydrogen plasma target of $5\mu m$ diameter. The target is placed equidistant from the six walls of the cubical simulation box of sides $20\mu m$. Thus, the target centre has the coordinates $(10, 10, 10)$ in microns. The laser has a Gaussian profile in the trans-

verse directions (X and Y) as well as in the longitudinal direction (Z), with the spatial full-width at half maxima (FWHM) being $10\mu m$ and the temporal FWHM being $33fs$. The laser peak intensity interacts with the centrally located target at $\approx 190fs$ and the time is referred to as the peak of interaction. With a wavelength of $1\mu m$, the laser has a frequency $\omega = 1.88 \times 10^{15} rad/s$ and the critical density at $n_c \simeq 1.112 \times 10^{21} cm^{-3}$. The peak laser intensity is varied from about $3.4 \times 10^{19} W cm^{-2}$ to $3.1 \times 10^{20} W cm^{-2}$ and correspondingly the normalized vector potential $(a_0 = \dfrac{eE_0}{\sqrt{2}m_e\omega c})$ also varied from $\simeq 5$ to 15. Here, E_0 is the peak laser field amplitude. The simulations are carried out with fixed spatial resolutions of 50nm and absorbing boundary conditions are applied for all six walls for both the fields and particles. Each cell is considered to contain 3 macroparticles each for electrons and protons and the temporal resolution is $0.2\omega_p^{-1}$. The spherical plasma target is considered to be cold initially and has a Gaussian-shaped variation in its density with the centre having the peak density n_{peak}. Such a density profile could be manipulated by pre-exploding a cryogenic solid hydrogen sphere $(n \approx 6 \times 10^{22} cm^{-3})$ with a laser pulse of lower intensity/ pre-pulse. The density equation is,

$$n(r) = n_{peak} exp \left[-\frac{1}{2} \left(\frac{r}{b} \right)^2 \right] \qquad (5.1)$$

where r is the distance from the centre of the sphere and $b \approx$ $0.425\times$ FWHM. The inhomogeneity FWHM $\approx 1.5\mu m$. The density profiles for the targets with varying peak densities are shown in Fig. 5.1(a). The horizontal lines define the relativistically critical density layer $\left(n_e = \gamma n_c = \sqrt{1 + \dfrac{a_0^2}{2}} n_c \right)$ of the targets for the corresponding laser strengths (a_0). The protons could be accelerated via different physical mechanisms when a non-uniform spherical plasma target is exposed to an intense laser beam. It is possible to attain high energetic collimated proton beams by suitably customizing the size of the target, steepness of density gradient, and intensity of the laser beam. Fig. 5.1(b) shows the variation of the maximum proton energy after saturation, on the peak

density n_{peak}. Here, we compared the final proton energies for three different laser strengths. It is seen that on average the maximum proton energy initially increases with an increase in n_{peak}. A sharp rise in the energy is visible at $n_{peak} = 12n_c$ for the cases with $a_0 = 7.07$ and 10.6. For $a_0 = 15$, the sharp rise in the maximum energy is seen in the case with $n_{peak} = 16n_c$. The energy is then further observed to attain a saturation upon reaching these maximum values for the corresponding cases. Depending on the steepness of the target density gradients, three separate regimes of proton motion can be identified. It has been observed that a small variation in the density gradient has shifted the proton acceleration mechanism from one form to another.
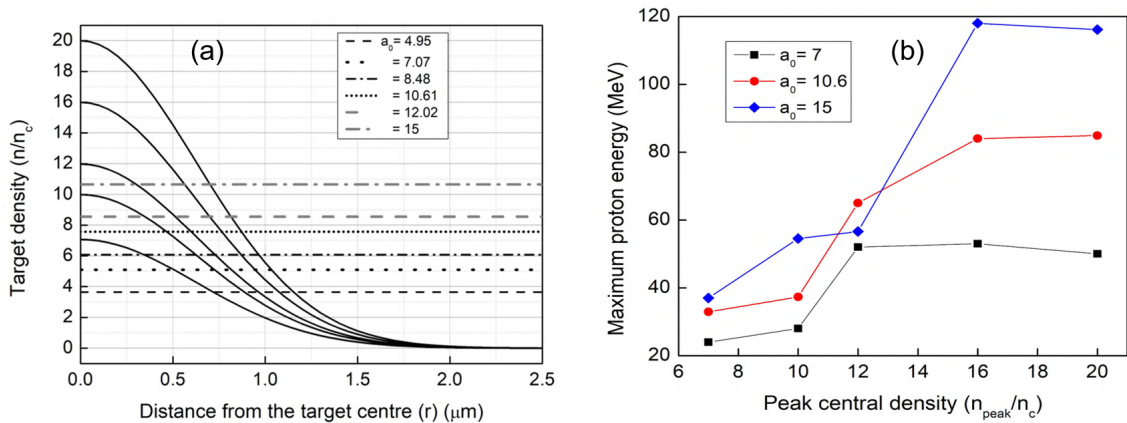

Figure 5.1:   (a)The density profiles of the target with varying central peak densities. The density drops radially in a Gaussian manner from the centre. The dotted horizontal lines show the relativistic critical density layer (γn_c) for different laser peak strengths. (b) gives the dependence of the maximum proton energy on the central peak density of the target. The three coloured lines represent three values of a_0.

5.3   Effect of density gradients

To explore the scope of such inhomogeneous targets, we have scanned over different regimes of density gradient and laser intensity. The study reveals that an intermediate density gradient may be identified which brings out interesting and desirable features of the accelerated protons.

5.3.1   Target with low density gradients

To study the effect of low gradients in the target density profile we considered those targets whose peak central densities $n_{peak} < 1.5\gamma n_c$ (see Fig. 5.1(a)). A typical example of such a situation is the target with peak density $n_{peak} = 7n_c$ which is hit by the laser with $a_0 = 7.07$. For this value of a_0, the critical density layer $\gamma n_c \simeq 5.1 n_c$, and therefore most of the target is relativistically transparent for the laser, except for a small volume at the centre with a diameter of $\approx 1\mu m$. This transparency leads to an overall expansion of the target which is discussed in Chapter 4 of the present thesis. A sharp proton wall accumulates at the rear end of the expanded target which gives an element of anisotropicity in the expansion mechanism, which is visible from the phase plot in Fig. 5.2(a). The protons could be seen attaining momenta in a favourable forward direction. The proton energy spectra [Fig 5.2(b)] shows spectral peaks at lower energies. The shape of the energy spectra resemble those of the ambipolar expansion. Thus, the plasma target undergoes an anisotropic ambipolar expansion which is due to the ponderomotive push of the laser in the low-density target.
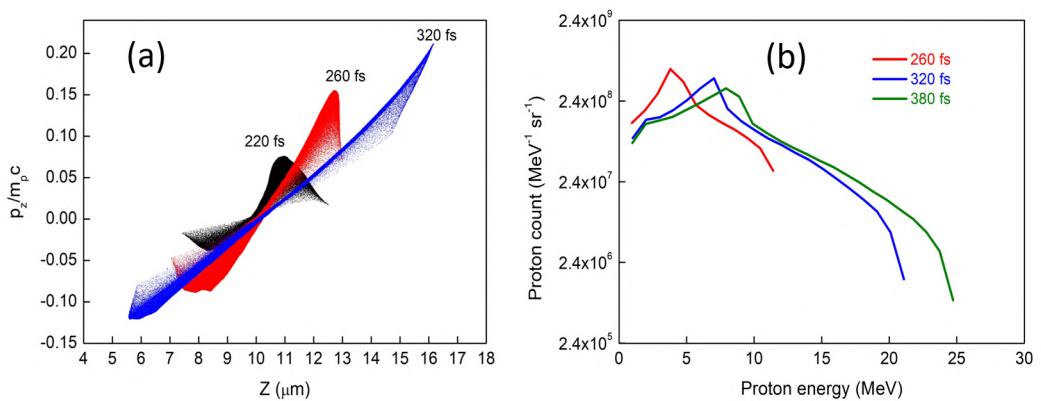

Figure 5.2:   (a) is the longitudinal phase plot along the laser axis (Z) at different times for the plasma target with central peak density $n_{peak} = 7n_c$ and the laser parameter $a_0 = 7.07$, (b) is the proton energy spectra at different times.

5.3.2   Target with intermediate density gradients

The intermediate density gradient region specified as central peak density "n_{peak}" satisfying $1.5\gamma n_c < n_{peak} < 2.5\gamma n_c$ reveals interesting physical effects due to the non-uniform Coulomb field experienced by the protons. For the case with $n_{peak} = 12n_c$ and peak laser intensity $I_0 = 1.37 \times 10^{20} W\,cm^{-2}$ corresponding to $a_0 \sim 7.07$, a sharp rise in the proton energy is observed in Fig. 5.1(b). As the laser gets stopped at the relativistically critical density layer, it transfers its energy partially to the electrons due to ponderomotive heating. The electrons get pushed forward whereas the protons remain quasi-stationary, giving rise to a space-charge field. An amplified electric field can be seen in Fig. 5.3(a), followed by a proton density steepening. The protons acquire high velocities near the centre of the target as seen in the longitudinal phase diagram of Fig. 5.3(b) at time 215 fs. With the evolution of time, these fast-moving protons create a strong axial field ahead of it [Fig. 5.3(c)]. This field appears at the decreasing density gradient regime at the rear half of the target $(Z > 10\mu m)$. This rise in the second electric field may be attributed to the non-uniformity among the core and the outer layers of the spherical target. As the electrons are pushed forward, the remaining protons experience non-uniform Coulombic repulsion at the central and the outer layers. As a result, the protons at the core acquire higher velocities than the outer protons, leading to overtaking among the protons [3, 4, 26]. This causes piling up of the protons leading to a density spike at $Z \approx 10.5\mu m$, triggering the formation of a strong collisionless shock. This is confirmed from the appearance of the knee-shaped structure indicated with an arrow in the proton phase plot of Fig. 5.3(d). The protons located at the upstream regions of the shock get reflected from the shock front, thus accelerating the protons to significantly high energies. The shock front coincides with the sharp proton peak that is seen in Fig. 5.3(c).

The shock and the subsequent proton reflection can be better visualised in the proton density in the central YZ plane in Fig. 5.4(a) at the shock formation time $\sim 230fs$. The strong longitudinal electric field formed as

132

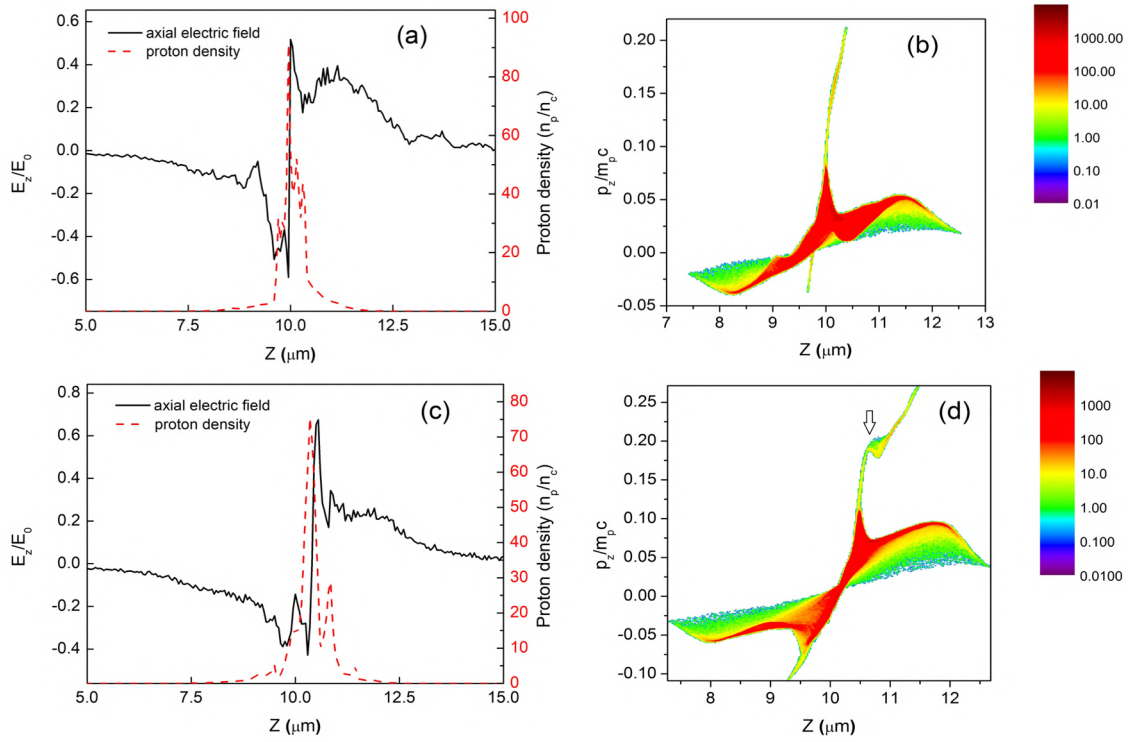Figure 5.3: (a) and (c) are the axial electric field (E_z) normalized by peak laser field E_0 (black-solid line) and the proton density (n_p) (red-dashed line) along the central laser axis. (b) and (d) are the respective longitudinal proton momenta along the central laser axis. The colour axis in (b) and (d) represents proton number in arb. units. The top row corresponds to time 214.9 fs and the bottom row corresponds to time 230.25 fs. Here, $a_0 = 7.07$ and $n_{peak} = 12n_c$. The arrow in (d) denotes the reflection from the shock front.

a result of the shock formation moves with the proton peak and can be seen in Fig. 5.4(b). Apart from the initial strong laser-induced field formed at $\sim 190 fs$ at the front side of the target, a secondary shock field starts developing at around $230 fs$ at the $Z > 10 \mu m$ (decreasing density region of the target). The slope of the propagating field gives the estimation of the shock velocity $v_s \approx 0.133c$. However in this regime, it is observed that the shock caused due to the proton-bunching moves with a velocity that is slowly increasing with time (similar to the observation in [4, 5, 26]). This is in contrast to the constant velocity exhibited by a laser-driven shock front. The increasing difference in density between the propagating shock front and the local protons, as the shock travels through the downward density gradient of the expanding target, may be responsible for the continuous gain in the velocity of the shock-front. The

proton energy spectra are shown for different times in Fig. 5.5(a). The spectra consist of two parts: a low energy part caused by the expansion of the background protons in the non-uniform density plasma, and a high energetic bunch due to the high-velocity shock reflected protons. The highest energetic protons are therefore a result of the reflections that occurred at the shock front. At the shock formation time (red curve), the shock reflected protons are accelerated with velocities $v_i = 2v_s \approx 0.266c$, which yields the maximum energy at around 33.3 MeV. At later stages of acceleration, the energy of the shock accelerated bunch broadens as those protons escape the target rear-side boundary, and accordingly the maximum proton energy also increases and reaches $\approx 55.5 MeV$ at saturation. Due to a steady drop in the density at the rear side, the influence of the sheath electric field on the dynamics of the accelerated protons is minimal. This effect is beneficial in reducing the energy spread of the emitted protons. Another desirable feature of this regime of proton acceleration is the strong collimation achieved as seen in Fig. 5.5(b) where the proton bunch is emitted from the target rear-side with a half-angle divergence less than 8 degrees. As the target core is much smaller than the spatial FWHM of the pulse, the expulsion of the electrons from the region causes a focusing effect and the low-divergence of the emitted beam may be attributed to the focusing effect created by the ponderomotive guiding of the electrons, as observed in [24].

As seen in Figs. 5.3 and 5.4, the shock originates at $Z > 10\mu m$ i.e. the negative gradient region of the density. When the high-density core reaches the downward density ramp in the target density, the fast-moving protons from the inner regions over-run the outer slow-moving protons moving with the expansion velocity. The density spike in the overtaking region causes the occurrence of the shock at a time which coincides with the wave-breaking time given in [27] for a Gaussian density target, as $t_{wb} = \dfrac{1}{\omega_{pi}} \sqrt{\dfrac{2n_{p0}}{max(n_e - n_p)}}$, where $\omega_{pi} = \sqrt{\dfrac{4\pi n_{peak}e^2}{m_p}}$ is the ion-plasma frequency and n_{p0} is the initial density at the centre, i.e. $n_{p0} \approx n_{peak}$. Also, $max(n_e - n_p)$ is the maximum value of the difference in the number densities of electrons and the protons. For the case at hand, this time is
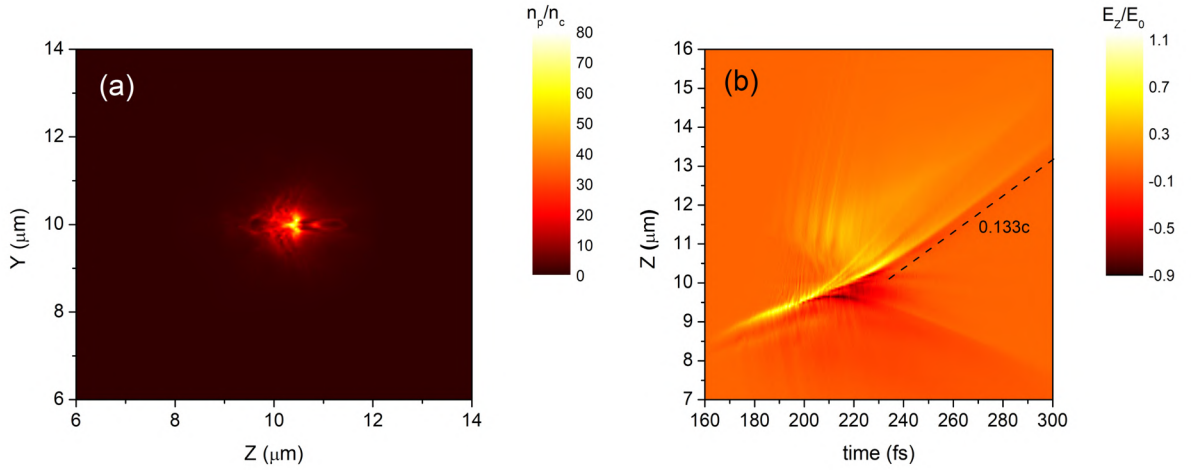
Figure 5.4: (a) The proton density snapshot along the central YZ plane at the shock formation time 230 fs; (b) The evolution of the longitudinal electric field (E_z) along the central Z-axis and time. The dotted line represents the shock front, and its slope $\approx 0.133c$ gives the shock velocity. The laser and plasma parameters are the same as Fig. 5.2
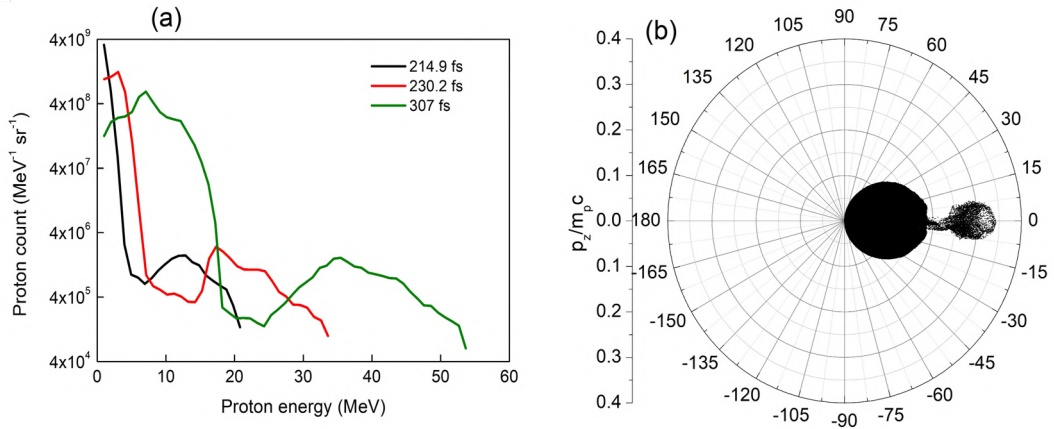

Figure 5.5: (a) The proton energy spectra at different times; (b) the angular divergence of the protons in degrees at 307 fs. The proton number in (a) is normalised by the total proton number. The laser and plasma parameters are the same as Fig. 5.2.

estimated as $t_{wb} \approx 9.9 fs$. The wave-breaking occurs only after the target heating is complete, i.e. around 214.9 fs. As a result, the wave-breaking time comes out to be $T_{wb} = 214.9fs + t_{wb} = 224.8fs$. On the other hand, the simulation shows that the wave-breaking driven shock (caused by the overtaking among the inner and outer protons) appears at around 230 fs. The slight difference of the time may be due to the fact that the model given by Mora [27] exclusively used the isothermal expansion for a one-dimensional plasma scenario.

Table 5.1: Comparison table for the theoretical estimation [27] and simulated value of T_{wb} for different cases

a_0	Peak density (n_c)	$max(n_e - n_i)$	T_{wb} from theory (fs)	T_{wb} from simulation (fs)
7.07	12	10.6	224.8	230
8.48	12	17.1	222.7	217
10.6	16	5.66	225.3	225.1
12	16	2.4	233.2	225.7
15	16	8.86	210	210

We have varied the target peak density as well as the laser peak intensity and identified a region where such intermediate density shocks are observed. The wave-breaking time is calculated theoretically and compared with the shock formation time from simulation. Table 5.1 gives the information on the theoretical [27] and simulated value of the wave-breaking time for the different cases. It is seen that the shock formation time matches fairly well with the theoretical calculation of wave-breaking time.

In this density regime, we obtained the case with $a_0 = 15$ with $n_{peak} = 16n_c$ to have the optimal proton beam in terms of energy and beam divergence. The protons with the highest energies are owed to the generation of extremely strong shock [Fig 5.6(a)] in the decaying density region of the target. The shock reflected protons are emitted out of the target with a high velocity which can be seen from the proton momentum plot Fig 5.6(b). In this case, we observed protons with energies as high as 118 MeV with a narrow peak (having energy spread $< 6\%$) at 102 MeV. This narrow bandwidth in the proton spectra represents those protons that are emitted out from the rear side of the target and therefore those protons could be directed for applications using proper guiding systems [Fig 5.6(c)].

To understand the influence of the spherical shape on the generation of the energetic protons, we simulated a pre-exploded planar target of thickness equal to the diameter of the sphere. The transverse dimension was chosen to be larger than the laser spot-size (transverse dimension $Y = 30\mu m$) instead of an infinitely extending foil due to limitations of
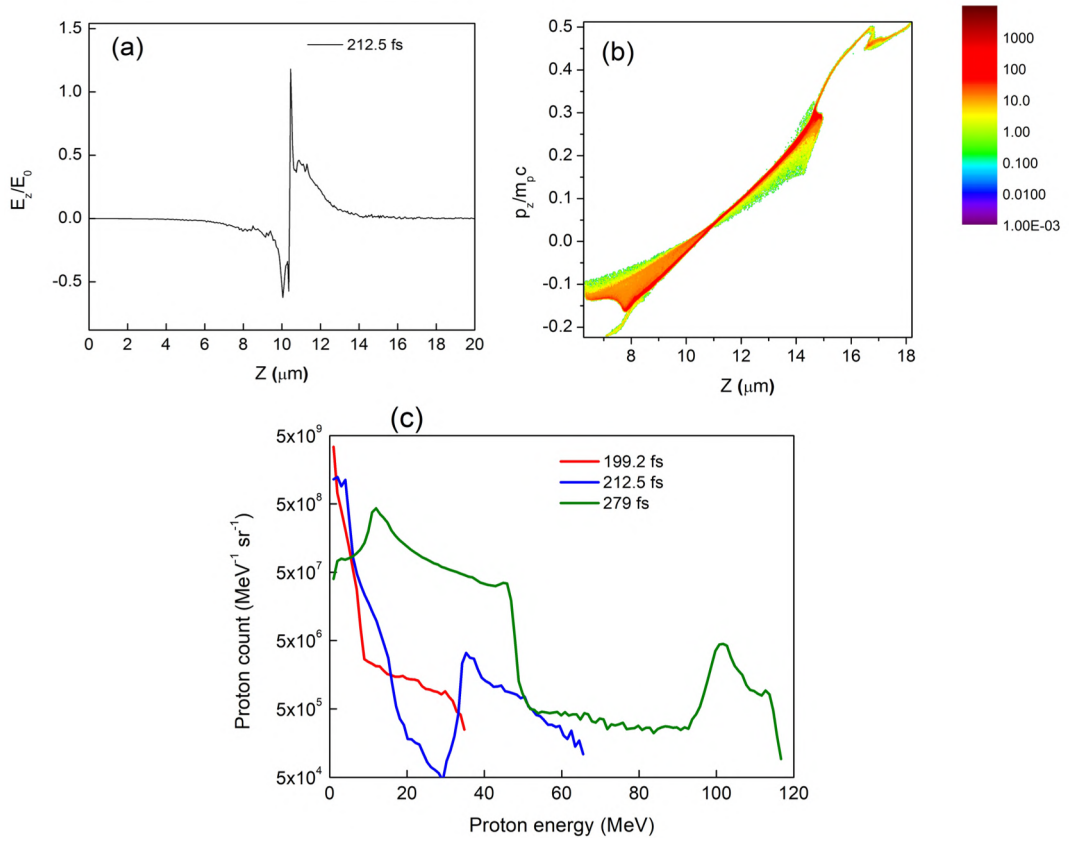
Figure 5.6: (a) The longitudinal electric field along the central laser axis at time 212.5 fs and (b) is the longitudinal proton momenta at time 265.6 fs for the target with $n_{peak} = 16n_c$ and $a_0 = 15$. (c) is the proton spectra at different times. The proton number in (c) is normalised by the total proton number.

3D simulations. We observed a suppression of the hot electron temprea-ture from $T_h = 5.7MeV$ in the spherical case to $T_h = 3.9MeV$ for the planar case [Fig. 5.7]. The transverse confinement provided by the spher-ical shape results in higher heating of the electrons. In the planar case, the laser pulse creates a hole-boring effect at the critical surface which pushes a dense bunch of protons from the front-side. The flat rear sur-face assists the generation of a stronger sheath field compared to the spherical case. Thus, the protons are accelerated in the planar case by a hole-boring field at the target front and are eventually pulled by a stronger sheath field.

The oscillating component of the non-linear ponderomotive force is ab-sent in case of circularly polarized lasers which reduces the transverse oscillation of the electrons. The electron density plot at 214.9 fs for a
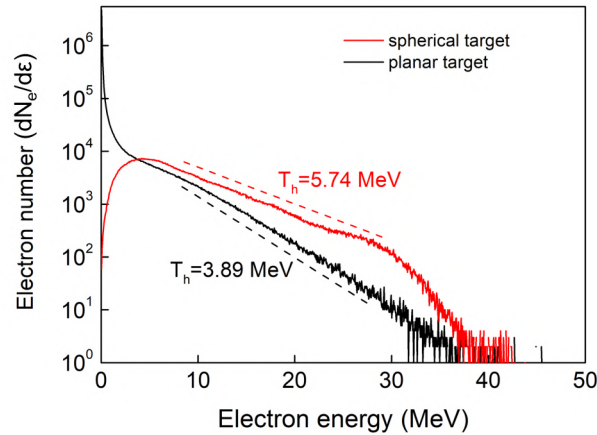
Figure 5.7: The electron energy spectra at 214.9 fs for the spherical (red) and the flat foil target (black). In both the cases, $a_0 = 7.07$ and $n_{peak} = 12n_c$. The slopes give the estimate of the hot electron temperatures.

linearly polarized (LP) and the circularly polarized (CP) lasers of equal intensities are shown in Fig. 5.8(a) and (b). The suppression of the oscillating component helps in an efficient expansion of the protons required for the formation of the shock. As the target considered in this study is pre-exploded, the expansion of the target is the reason behind the shocks that are developed inside the target. It is observed that the proton expansion rate is slow in case of LP laser in comparison to a CP laser. Non-uniform expansion velocity of the protons and the resulting wave-breaking may not be achieved with LP due to this slow expansion. This is indicated by the absence of the high energetic peak in the proton spectra in case of LP [Fig. 5.8(c)]. As a result, the emitted high-energetic proton bunch observed in case of the CP laser is not seen in the LP case. It has been observed that even with the suppression of the oscillating component of the ponderomotive force, the electron energy absorption efficiency can be high with the use of focused CP lasers [28]. This may be a reason for the generation of strong shocks in our cases with circularly polarized lasers.
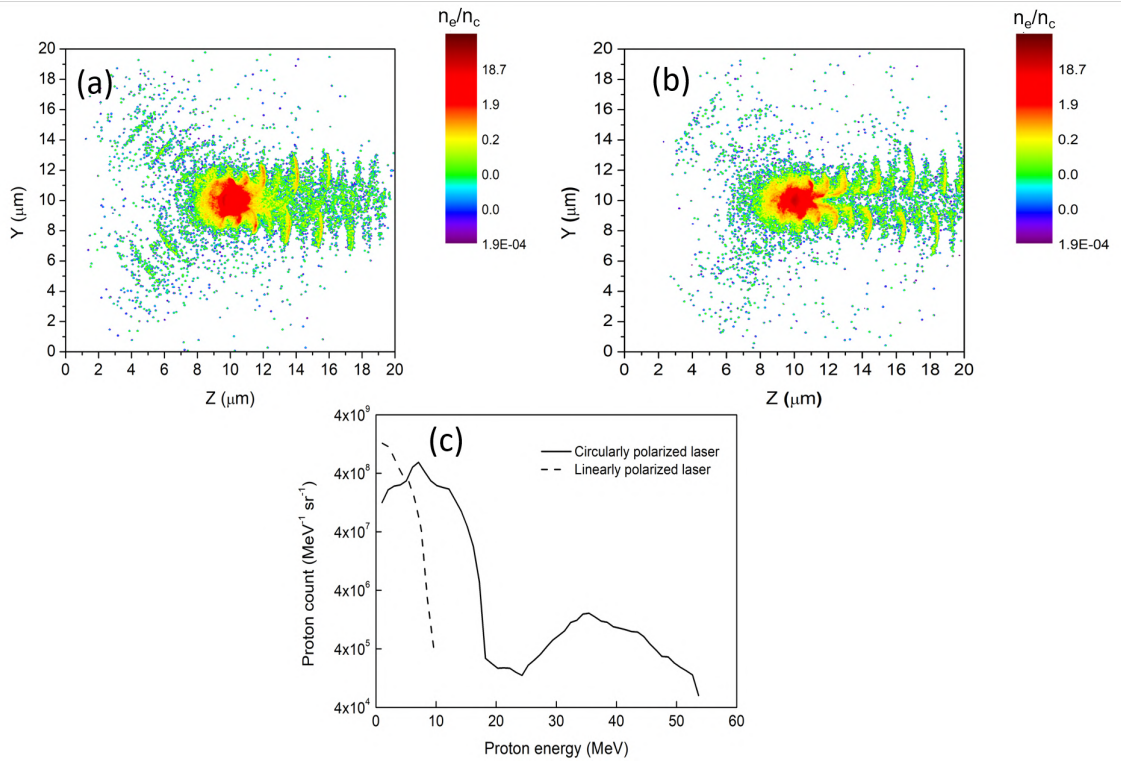
Figure 5.8: Electron density distribution in the central YZ plane for the (a) LP and (b) CP cases. (c) the proton energy spectra at the saturation times 307 fs for the circularly polarized case (solid line) and 506.6 fs for the linearly polarized case (dotted line). In both the cases, $a_0 = 7.07$ and $n_{peak} = 12n_c$.

5.3.3 Target with high density gradients

This third regime of ion acceleration is obtained for the high-density targets where $n_{peak} > 2.5\gamma n_c$. We consider a target with diameter $n_{peak} = 16n_c$ and laser pulse with $a_0 = 7.07$. In this regime, three processes seem to take place in phases. In the first phase, the hole-boring mechanism is caused by the laser-piston action on the steep density gradient at the target front-side. The peak of the laser pulse pushes the protons of the increasing density ramp inwards and produces two diverging beams of protons upon colliding with the dense centre of the target [Fig 5.9(a)]. The propagating proton bunch finally transforms into a shock, and when the resultant electrostatic potential becomes high enough, the shock front starts reflecting protons in its upstream region [Fig. 5.9(b)]. This is the standard collisionless shock acceleration driven by the laser pulse and is the second phase of the proton dynamics. The

abrupt jump in the density signifies the shock generation, and from the hydrodynamic predictions [29], the shock formation conditions are satisfied when the density of the downstream region is higher than the density of the upstream region. Considering the upstream plasma to be at rest, its density $n_0 > \left(\dfrac{k_{ad} - 1}{k_{ad} + 1}\right) \gamma n_c$. Here, k_{ad} is the adiabatic coefficient. For the present case, this condition is satisfied as $n_0 > 1.28 n_c$. The third phase of the acceleration arises due to the presence of a steep density gradient at the rear side of the target. The formation of the electrostatic sheath field due to the accumulation of the hot electrons pulls the shock reflected protons with a non-uniform velocity depending upon their distances from the sheath field. This effect is almost similar to that of a sharp plasma-vacuum interface of a uniform density target. The effect of the sheath field is stronger for high-density gradients compared to the former two cases and can be seen in the phase plot of Fig. 5.10(a). The proton density figure 5.9(c) shows the dissolution of the strong shock front due to the presence of the sheath field. The proton energy spectra [Fig 5.10(b)] at different times show distinct plateau regions which is a signature of CSA. The spectra broaden as a result of the non-uniform pull of the sheath field. Small peaks of mono-energetic protons are observed in the low energy end of the spectra which are caused due to the shock shells created in the decreasing density regions of the target.

A comparison of the shock regime attained in these high-density cases is made with that of the model used in [22]. There, a similar type of pre-exploded target was interacted with linearly polarized pulse, and the acceleration regime for the highest energy proton cases was identified to be Collisionless shock acceleration. As the simulation model is somewhat similar to ours (although the density profile we used for our cases is Gaussian), we recorded the maximum proton energy at the shock formation time as a function of the parameter (I_0/n_0) and it is compared with the theoretical model in [22] [Fig. 5.11(a)]. The maximum energy scales in a similar manner as the CSA scheme reported
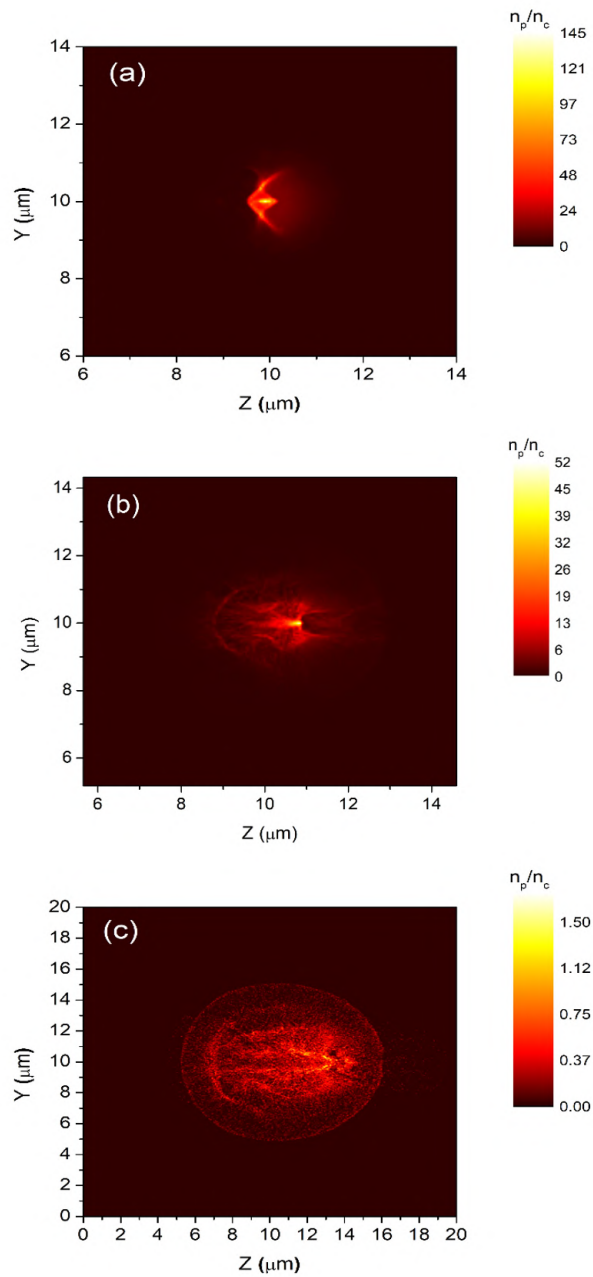
Figure 5.9: The proton density in the central YZ plane at times (a) 212.7 fs, (b) 252.6 fs (shock reflection) and (c) 319 fs. Here, $a_0 = 7.07$ and $n_{peak} = 16n_c$.

there. In addition, it is seen that all the data points yield maximum proton energies higher than those given by the predictions of the model used in [22]. In Fig. 5.11(b), a similar comparison plot is made with [22] but now using linearly polarized laser. It is seen that the points matches closely with the model used there. Thus, laser polarization is seen to affect the production of energetic protons and the difference in
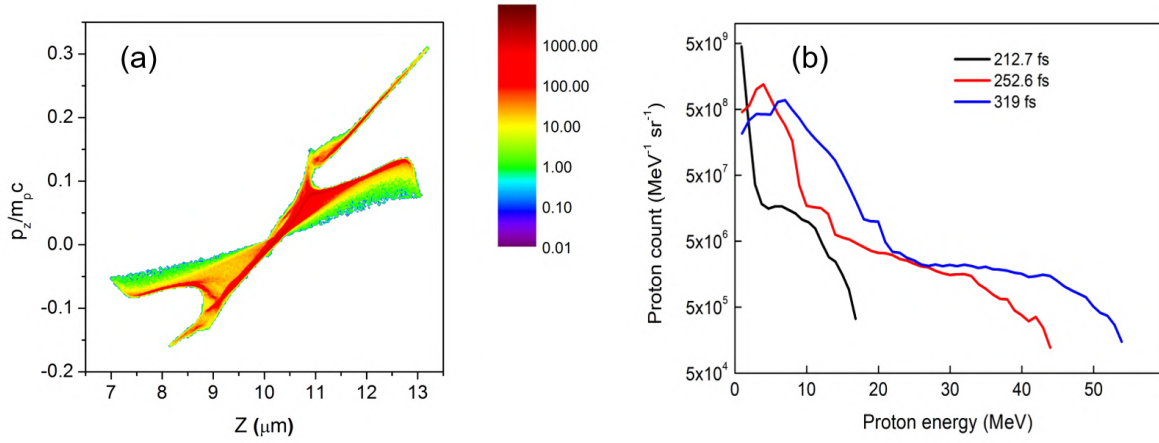
141

Figure 5.10:   (a) The longitudinal phase plot at the shock formation time 252.6 fs. (b) The proton energy spectra at different times. The laser and plasma parameters are same as Fig. 5.9.
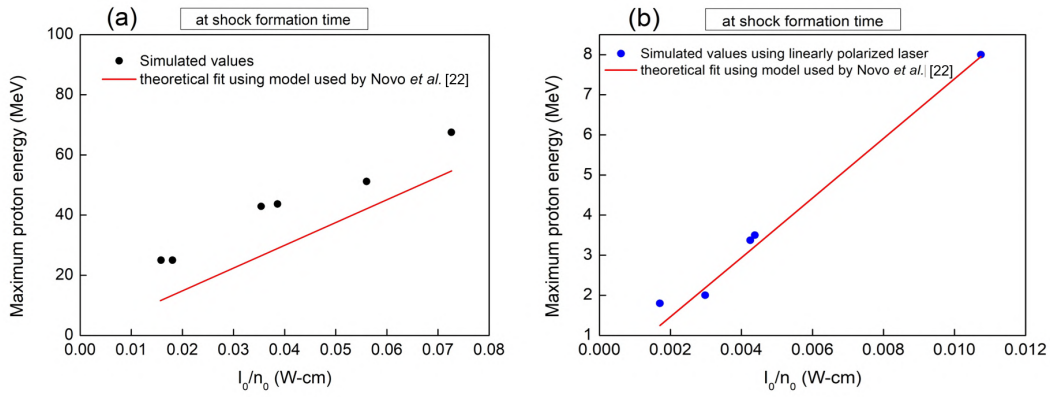

Figure 5.11:   (a-b) The maximum proton energy at the shock formation time for the different cases (in the high-density regime) as a function of the parameter (I_0/n_0). The black circles in (a) give the simulated values using the circularly polarized laser and the blue circles in (b) give the simulated values using the linearly polarized laser. The red straight lines in (a) and (b) is obtained from the model equation in [22].

the energy values from the CSA model seen in Fig. 5.11(a) is due to the circular polarization of the pulse used in our work. This observation suggests that the circular polarization of the laser helps in the generation of proton bunches with higher energies compared to a linearly polarized laser in the explored parameter regime. The circular polarization of the laser aids a steady expansion of the target by suppressing the oscillating component of the electron ponderomotive force. Along with a stronger proton absorption efficiency, the use of a focused circularly polarized

laser has increased the electron absorption efficiency significantly in multi-dimensional PIC simulation reported in [28]. This might be the reason for the development of strong shocks in the circularly polarized cases observed in our work that leads to the production of protons with higher energies compared to linearly polarized lasers. It is to be noted here that accelerating protons to similar energies using the low-density shock mechanisms using a circularly polarized pulse require much lower laser intensities compared to those used in [22]

5.4   Comparison between the different acceleration regimes

It is seen that the underlying interaction and ion acceleration mechanism depends greatly on the density gradient of the target. In this work, we have achieved three separate regimes of proton dynamics with the source of acceleration being the result of a number of separate mechanisms. A small change in the density gradient has displayed a big change in the final energies of the protons.

Fig 5.12 shows the temporal evolution of the longitudinal electric field along the laser axis, for the three regimes. Two peaks in the electrostatic fields are formed for the intermediate and high-density cases. The first one is formed at the front side of the target and is due to the momentum transfer from the laser pulse, and the second one is formed at the target bulk due to the shock formation. From Fig. 5.12(b-c) it is seen that the shock field is present in the cases with the intermediate and high-density gradients, however, the shock field is greater for intermediate densities. This field is formed due to the over-running among the protons in the decreasing gradient of density at the rear side half of the target. The time delay between the two peaks varies with the density gradients, and it is seen that the delay between the peaks increases as the gradient becomes steeper.
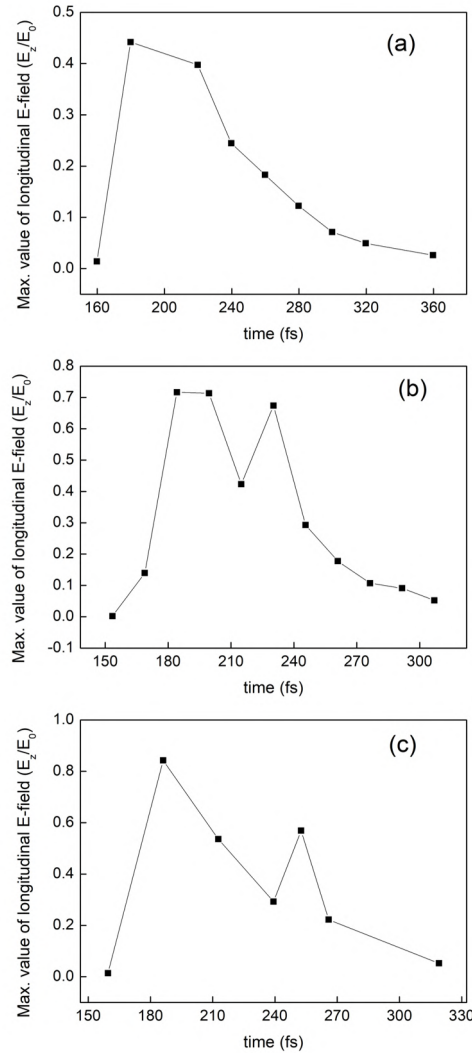
Figure 5.12: (a-c) The temporal evolution of the longitudinal electric field along the central laser axis for the targets having low, intermediate and, high-density gradients respectively. The figures are for the cases with $a_0 = 7.07$ and (a)$n_{peak} = 7n_c$, (b) $n_{peak} = 12n_c$ and (c)$n_{peak} = 16n_c$ respectively. These are typical figures and other values of a_0 and n_{peak} that fall under a particular regime of mechanism also follow a similar trend in their respective figures.

5.5   Proton energy scaling

For the efficient expansion and shock formation inside the target, therefore it is necessary to have a scaling between the target peak density and the laser strength. As a stronger laser pulse is expected to increase the laser to proton energy conversion efficiency, similarly it is also required that the density gradient remain intermediate for both the expansion and the eventual shock to play their parts in the proton dy-

144

namics. We have varied the laser peak intensities and the three different regimes are marked in a target peak density-laser intensity space [Fig 5.13(a)]. The blue region (squares) marks the expansion regime with the lowest density gradients. The yellow region (triangles) corresponds to the intermediate regime. The red region (circles) has the highest density gradients. To attain an energy scaling law, in Fig 5.13(b), the maximum proton energies are recorded as a function of the parameter (I_0/n_{peak}). the linear fitting gives a scaling of the two different shock regimes (high-density gradients: (circles), and intermediate-density gradients: (triangles) on the parameter I_0/n_{peak}. From the figure, the high-density regime has a scaling law: $\varepsilon_{max} \sim \left(\dfrac{I_0}{n_{peak}}\right)^{0.76}$. Similarly, the hybrid shock in the intermediate density gradients has a scaling law: $\varepsilon_{max} \sim \left(\dfrac{I_0}{n_{peak}}\right)^{0.94}$.
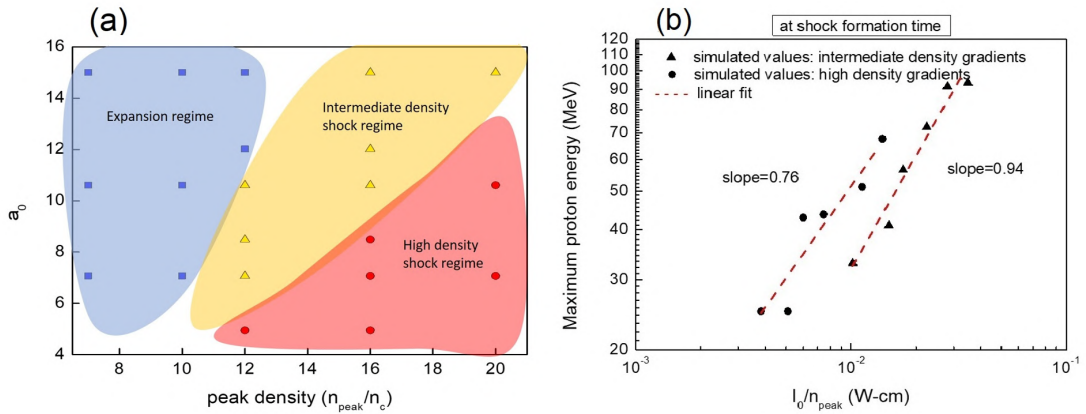

Figure 5.13: (a) The three regimes of ion acceleration are marked in space consisting of n_{peak} and a_0. (b) The maximum proton energies obtained are recorded for different values of the parameter (I_0/n_{peak}) at the shock formation time for the intermediate and high-density gradients. The black circles are those points that have $n_{peak} > 2.5\gamma n_c$. The black triangles are those values that have intermediate density gradients ($1.5\gamma n_c < n_{peak} < 2.5\gamma n_c$). The dotted straight lines give a linear fitting of the points.

5.6 Conclusion

In this chaper, we have utilised a pre-deformed spherical hydrogen plasma target with a radially Gaussian density profile to produce high energetic proton bunches, using a circularly polarized femtosecond laser pulse. This work extends our study from the previous work [19] where

we found that a Gaussian density variation in the target promotes the generation of higher energetic and collimated beams of protons. In this study, we scanned the parameters and established a region in the relativistically critical and overdense regime where a change in the density steepness has resulted in the manifestation of three regimes of proton acceleration. The important findings of this study may be summarised as follows:

1. For density gradients $(n_{peak} > 1.5\gamma n_c)$, shock formation is the principal mechanism in the proton motion. Other supplementary mechanisms are occurring alongside the formation of shocks due to the electrostatic fields inside the target. Therefore, the final proton energies are governed by the cumulative effects of all the underlying processes.

2. With intermediate density gradients, i.e. $1.5\gamma n_c < n_{peak} < 2.5\gamma n_c$, the steepness of the density is ideal for the occurrence of a wave-breaking shock in the rear half of the target sphere. Such shocks are caused due to the overrunning of the outer, slow-moving protons by the inner fast protons. Moreover, the overall expansion of the target aids the shock reflected upstream protons to reach higher energies. The emitted proton bunch has a limited energy spread and is due to a relatively suppressed TNSA field in the downward density gradient compared to a steep plasma-vacuum density drop. The resultant protons have a low divergence and narrow energy bandwidth with mean energies exceeding 100 MeVs using a laser of comparatively lower intensity $I_0 \sim 10^{20}Wcm^{-2}$.

3. When the density gradients are further increased $(n_{peak} > 2.5\gamma n_c)$, the underlying mechanisms of proton acceleration are initially hole-boring in the dense core of the target. At a later stage, CSA comes into action and accelerates the protons to higher energies. The steep gradient at the rear-side creates a stronger sheath field, almost similar to the case of a sharp plasma-vacuum interface. As a result, the shock accelerated protons attain a broad energy spectrum

due to the additional non-uniform pull of the rear-surface electrostatic field.

4. For low density gradients ($n_{peak} < 1.5\gamma n_c$), the expansion of the target plays the prime role in the proton dynamics. The protons expand with a preferential flow along the forward laser direction. A gentler density slope in the rear side resists the generation of efficient shocks.

5. A scaling of the proton energies with the peak intensity and density for the two types of shocks formed in the intermediate and the high-density cases is done. It is seen that the intermediate density shocks have a stronger dependence with $\varepsilon_{max} \sim \left(\dfrac{I_0}{n_{peak}}\right)^{0.94}$ compared to $\varepsilon_{max} \sim \left(\dfrac{I_0}{n_{peak}}\right)^{0.76}$ for high density gradients.

6. The comparison with an extended flat target shows yields reduced proton energies compared to a spherical mass-limited plasma target. The transverse confinement of the electrons in the spherical target supports an effective recirculation of the hot electrons.

7. It is found that the acceleration of the protons from the shocks in both the intermediate and high density gradient regimes is crucially dependent on the polarization of the laser pulse. The circular polarized laser aids a stronger expansion of the exploded target compared to the linear polarized laser. As a result, the formation of the shock due to the non-uniform velocities of the plasma ions may not take place in the linearly polarized cases which suppresses the resultant proton energies. For the parametric region discussed in this study, we find circularly polarized pulses to be effective in the generation of energetic protons with high proton flux.

The results of this work suggests that a Gaussian density gradient in a spherical target with appropriate tuning and refinement may be utilised as a contester in laser plasma ion accelerations. Adopting proper diagnosis in terms of laser and target parameters are therefore essential in the harnessing of high quality ion beams for application purposes.

Bibliography

[1] Silva, L. O., Marti, M., Davies, J. R., Fonseca, R. A., Ren, C., Tsung, F. S., and Mori, W. B. Proton shock acceleration in laser-plasma interactions. *Phys. Rev. Lett.*, 92(1):015002, 2004.

[2] Fiuza, F., Stockem, A., Boella, E., Fonseca, R., Silva, L., Haberberger, D., Tochitsky, S., Mori, W., and Joshi, C. Ion acceleration from laser-driven electrostatic shocks. *Phys. Plasmas*, 20(5):056304, 2013.

[3] Grismayer, T. and Mora, P. Influence of a finite initial ion density gradient on plasma expansion into a vacuum. *Physics of Plasmas*, 13(3):032103, 2006.

[4] Peano, F., Fonseca, R., and Silva, L. Dynamics and control of shock shells in the coulomb explosion of very large deuterium clusters. *Physical review letters*, 94(3):033401, 2005.

[5] Peano, F., Fonseca, R., Martins, J. L., and Silva, L. O. Controlled shock shells and intracluster fusion reactions in the explosion of large clusters. *Physical Review A*, 73(5):053202, 2006.

[6] Fiúza, F., Stockem, A., Boella, E., Fonseca, R., Silva, L., Haberberger, D., Tochitsky, S., Gong, C., Mori, W. B., and Joshi, C. Laser-driven shock acceleration of monoenergetic ion beams. *Physical Review Letters*, 109(21):215001, 2012.

[7] Boella, E., Fiúza, F., Novo, A. S., Fonseca, R., and Silva, L. Ion acceleration in electrostatic collisionless shock: on the optimal density profile for quasi-monoenergetic beams. *Plasma Physics and Controlled Fusion*, 60(3):035010, 2018.

[8] d'Humières, E., Antici, P., Glesser, M., Boeker, J., Cardelli, F., Chen, S., Feugeas, J., Filippi, F., Gauthier, M., Levy, A., et al. Investigation of laser ion acceleration in low-density targets using exploded foils. *Plasma Physics and Controlled Fusion*, 55(12):124025, 2013.

[9] Antici, P., Boella, E., Chen, S., Andrews, D., Barberio, M., Böker, J., Cardelli, F., Feugeas, J., Glesser, M., Nicolaï, P., et al. Acceleration of collimated 45 mev protons by collisionless shocks driven in low-density, large-scale gradient plasmas by a 10 20 w/cm 2, 1 μm laser. *Scientific reports*, 7(1):1–9, 2017.

[10] Chen, S., Vranic, M., Gangolf, T., Boella, E., Antici, P., Bailly-Grandvaux, M., Loiseau, P., Pépin, H., Revet, G., Santos, J., et al. Collimated protons accelerated from an overdense gas jet irradiated by a 1 μm wavelength high-intensity short-pulse laser. *Scientific Reports*, 7(1):1–12, 2017.

[11] Boella, E., Bingham, R., Cairns, R. A., Norreys, P., Trines, R., Scott, R., Vranic, M., Shukla, N., and Silva, L. Collisionless shock acceleration in the corona of an inertial confinement fusion pellet with possible application to ion fast ignition. *Philosophical Transactions of the Royal Society A*, 379(2189):20200039, 2021.

[12] Schwoerer, H., Pfotenhauer, S., Jäckel, O., Amthor, K.-U., Liesfeld, B., Ziegler, W., Sauerbrey, R., Ledingham, K., and Esirkepov, T. Laser-plasma acceleration of quasi-monoenergetic protons from microstructured targets. *Nature*, 439(7075):445, 2006.

[13] Fedeli, L., Formenti, A., Bottani, C. E., and Passoni, M. Parametric investigation of laser interaction with uniform and nanostructured near-critical plasmas. *The European Physical Journal D*, 71(8):1–8, 2017.

[14] Fedeli, L., Formenti, A., Cialfi, L., Pazzaglia, A., and Passoni, M. Ultra-intense laser interaction with nanostructured near-critical plasmas. *Scientific reports*, 8(1):1–10, 2018.

[15] Willingale, L., Nagel, S., Thomas, A., Bellei, C., Clarke, R., Dangor, A., Heathcote, R., Kaluza, M., Kamperidis, C., Kneip, S., et al. Characterization of high-intensity laser propagation in the relativistic transparent regime through measurements of energetic proton beams. *Physical review letters*, 102(12):125002, 2009.

[16] Passoni, M., Zani, A., Sgattoni, A., Dellasega, D., Macchi, A., Prencipe, I., Floquet, V., Martin, P., Liseykina, T., and Ceccotti, T. Energetic ions at moderate laser intensities using foam-based multi-layered targets. *Plasma Physics and Controlled Fusion*, 56(4):045001, 2014.

[17] Prencipe, I., Sgattoni, A., Dellasega, D., Fedeli, L., Cialfi, L., Choi, I. W., Kim, I. J., Janulewicz, K. A., Kakolee, K., Lee, H. W., et al. Development of foam-based layered targets for laser-driven ion beam production. *Plasma Physics and Controlled Fusion*, 58(3):034019, 2016.

[18] Sgattoni, A., Londrillo, P., Macchi, A., and Passoni, M. Laser ion acceleration using a solid target coupled with a low-density layer. *Physical Review E*, 85(3):036405, 2012.

[19] Bhagawati, A. and Das, N. Laser-accelerated protons using density gradients in hydrogen plasma spheres. *Journal of Plasma Physics*, 87(4), 2021.

[20] Andreev, A., Sonobe, R., Kawata, S., Miyazaki, S., Sakai, K., Miyauchi, K., Kikuchi, T., Platonov, K., and Nemoto, K. Effect of a laser prepulse on fast ion generation in the interaction of ultra-short intense laser pulses with a limited-mass foil target. *Plasma physics and controlled fusion*, 48(11):1605, 2006.

[21] Lécz, Z. and Andreev, A. Shock wave acceleration of protons in inhomogeneous plasma interacting with ultrashort intense laser pulses. *Physics of Plasmas*, 22(4):043103, 2015.

[22] Novo, A. S., Kaluza, M., Fonseca, R., and Silva, L. Optimizing laser-driven proton acceleration from overdense targets. *Scientific reports*, 6:29402, 2016.

[23] Hilz, P., Ostermayr, T., Huebl, A., Bagnoud, V., Borm, B., Bussmann, M., Gallei, M., Gebhard, J., Haffa, D., Hartmann, J., et al.

Isolated proton bunch acceleration by a petawatt laser pulse. *Nature communications*, 9(1):1–9, 2018.

[24] Huebl, A. *PIConGPU. Predictive simulations of laser-particle accelerators with manycore hardware.* 2019.

[25] Upadhyay, A., Patel, K., Rao, B., Naik, P., and Gupta, P. Three-dimensional simulation of laser–plasma-based electron acceleration. *Pramana*, 78(4):613–623, 2012.

[26] Kaplan, A. E., Dubetsky, B. Y., and Shkolnikov, P. Shock shells in coulomb explosions of nanoclusters. *Physical review letters*, 91(14):143401, 2003.

[27] Mora, P. Collisionless expansion of a gaussian plasma into a vacuum. *Physics of plasmas*, 12(11):112102, 2005.

[28] Liseikina, T. V., Prellino, D., Cornolti, F., and Macchi, A. Ponderomotive acceleration of ions: Circular versus linear polarization. *IEEE transactions on plasma science*, 36(4):1866–1871, 2008.

[29] Fiúza, F., Fonseca, R., Tonge, J., Mori, W. B., and Silva, L. Weibel-instability-mediated collisionless shocks in the laboratory with ultraintense lasers. *Physical Review Letters*, 108(23):235004, 2012.